

# Facile fabrication of $Tl_4HgI_6$ nanostructures as a novel antibacterial and antibiofilm agents

**Maryam Karami**

UNIVERSITY OF KASHAN

**Mojgan Ghanbari**

UNIVERSITY OF KASHAN

**Omid Amiri**

UNIVERSITY OF RAPARINE

**MASOUD SALAVATI-NIASARI** (✉ [Salavati@kashanu.ac.ir](mailto:Salavati@kashanu.ac.ir))

University of Kashan

**Somaye Rashki**

Kashan University of Medical Sciences

---

## Research

**Keywords:** Anti-biofilm, Bactericidal activity,  $Tl_4HgI_6$ , Nanostructure, Co-precipitation

**Posted Date:** November 13th, 2020

**DOI:** <https://doi.org/10.21203/rs.3.rs-101144/v1>

**License:**   This work is licensed under a Creative Commons Attribution 4.0 International License.

[Read Full License](#)

---

# Abstract

In the present study, Ti<sub>4</sub>HgI<sub>6</sub> nanostructures have been successfully fabricated through a simple precipitation route. The impact of Ti stoichiometric ratio to HgI<sub>2</sub>, and kind of surfactants was explored on purity, structure, and shape of samples. The as-fabricated Ti<sub>4</sub>HgI<sub>6</sub> was characterized via XRD, EDX, FESEM, TEM, HRTEM, and Raman spectroscopy. Raman spectrometry corroborated the XRD outcomes, and revealed that the Ti<sub>4</sub>HgI<sub>6</sub> nanoparticles were successfully fabricated. The structure, shape, and scale of the products were studied through FESEM images. It was observed that different factors have a notable aspect on the morphology and size of the products. The maximum antibacterial activity of Ti<sub>4</sub>HgI<sub>6</sub> was perceived against *S. aureus*, *E. coli* and *M. catarrhalis*. These outcomes demonstrate that Ti<sub>4</sub>HgI<sub>6</sub> displays efficient bactericidal activity against Gram-positive and Gram-negative microorganisms. The anti-biofilm activity revealed that the best reduction of biofilm was recognized in higher Ti<sub>4</sub>HgI<sub>6</sub> concentrations (2×MIC). Ti<sub>4</sub>HgI<sub>6</sub> at 2×MIC concentration inhibits biofilm production by *S. aureus* and *E. faecalis* with an inhibition percentage of 95% and 90%, respectively.

## 1- Introduction

Antibacterial resistance has appeared as a worldwide menace to community health and has turned to the principal reason for fatality. *Staphylococcus aureus* is the principal cause of nosocomial diseases correlated with enhanced incidence [1]. Methicillin-resistant *Staphylococcus aureus* is entirely accountable for multiple serious nosocomial diseases in humans which enhances the therapy continuation and remedial expenses [2]. They are identified to induce diverse moderate to persistent diseases in animals. Persistence against the final usage of medicines including, linezolid and vancomycin have appeared in the clinical isolates of *Staphylococcus aureus* which possess more aggravated the situation [3]. Moreover, the resistance issue is prevented via the capability of *Staphylococcus aureus* to produce biofilms on abiotic and biotic superficies mainly on various therapeutic implanted devices [4]. *Staphylococcus aureus* biofilm formation is an even more important menace owing to enhanced sensitivity against the host defense system and antibacterial [5]. Biofilms are complicated to use and examined as a microbial repository for distribution to different body sections [6]. These contagions may be caused by replacing the implanted medical device, thereby making extended suffering at the patient's additional medical expenses [7]. By growing fatality rate because of AMR, there is a necessity to seek new approaches to improve antimicrobials to resist biofilms and multidrug-resistance associated infections [8]. Scientists are utilizing different strategies to recognize novel compounds or novel antibiotics with antibacterial activity. Several preventions of diverse passage, antibacterial peptides obtained from organic and inorganic manufactured combination, and various ecosystems by antibacterial activity have been recognized and investigated [9, 10]. In search of discovering novel materials having antibacterial activity has attracted much attention.

Fabrication of an advanced group of nano-materials amidst distinctive formation and optoelectronic/electronic features is one example of the extensive demands inside the factual community. For a while, scientists dealt with the unique crystal semi-conductive substances with an

extended forbidden band. The extended forbidden band semi-conductors possess great denseness that can apply within many areas, including the non-expansion of nuclear materials, medical imaging, homeland security, etc [11, 12]. One of the interesting and inspiring features is a classification of  $B_4AC_6$  crystalline solid, with  $B = \text{In, Tl}$ ,  $A = \text{Pb, Hg, Cd, Ge, Zn, Mg}$ , and  $C = \text{Cl, Br, I}$ . Lately, semi-conductor ternary iodides including,  $\text{Tl}_4\text{HgI}_6$ ,  $\text{Tl}_4\text{CdI}_6$ ,  $\text{Tl}_4\text{PbI}_6$ , and  $\text{In}_4\text{CdI}_6$ , have been drawn consideration to the scientists [13]. A large number of ternary halides, for instance,  $\text{Tl}_4\text{HgI}_6$  discloses a noteworthy conductivity potential and exposes the solidity ionic conduction including heavy metals (like Tl) [12-17]. Additionally,  $\text{Tl}_4\text{HgI}_6$  shows potential applications in temperature sensors, ionizing radiation detectors, and ionic conductors.  $\text{Tl}_4\text{HgI}_6$  is a direct forbidden band semi-conductor with an energy gap of about 2.150 eV and reveals cathode luminescence and photoluminescence [18]. To date,  $\text{Tl}_4\text{HgI}_6$  has been fabricated via the Bridgman–Stock burger method and solid-state route below hard conditions and high temperature [19, 20]. Precipitation is an efficient procedure for fabrication nanomaterials since this method furnishes a facile, clean and suitable approach, and possesses numerous benefits, including low cost, simple component adjustment, eco-friendly, and high homogeneity of the acquired nanomaterials [21].

In the current report,  $\text{Tl}_4\text{HgI}_6$  nanostructures were fabricated via the co-precipitation route as a new method that furnishes the small size and high homogeneity product. The effects of multiple factors including, distinct surfactants and molar concentration ratio of TII to  $\text{HgI}_2$  were examined on purity and structure of samples. Finally, the samples were examined to reach the best position via EDX, XRD, SEM, Raman spectrometry and TEM for the fabrication of the desired product. The antibacterial and anti-biofilm activities of  $\text{Tl}_4\text{HgI}_6$  were studied. The outcomes demonstrate that  $\text{Tl}_4\text{HgI}_6$  displays efficient bactericidal activity against Gram-positive and Gram-negative microorganisms.

## 2- Experimental

### 2-1- Precursors

Each alchemic agent utilized in the present paper was provided within the analytic standard. Mercury(II) acetate ( $\text{Hg}(\text{COOH})_2$ ), Thallium(I) nitrate ( $\text{TlNO}_3$ ), Sodium dodecyl sulfate (SDS), polyvinyl pyrrolidone (PVP-25000), Lithium iodide ( $\text{LiI} \cdot 2\text{H}_2\text{O}$ ), Ethylenediaminetetraacetic acid (EDTA), Sodium salicylate ( $\text{NaHSal}$ ), and Hexadecyltrimethylammonium bromide (HTAB) were acquired from Merck Company and utilized without more purification. The rhodamine B ( $\text{C}_{28}\text{H}_{31}\text{ClN}_2\text{O}_3$ ), methyl orange ( $\text{C}_{14}\text{H}_{14}\text{N}_3\text{NaO}_3\text{S}$ ), methyl violet ( $\text{C}_{24}\text{H}_{28}\text{N}_3\text{Cl}$ ), acid black 1 ( $\text{C}_{22}\text{H}_{14}\text{N}_6\text{Na}_2\text{O}_9\text{S}_2$ ) and thymol blue ( $\text{C}_{27}\text{H}_{30}\text{O}_5\text{S}$ ) were obtained from Sigma-Aldrich and utilized as object contaminates for exploring of the photocatalytic performance of  $\text{Tl}_4\text{HgI}_6$  nanostructures.

### 2-2- Preparation of starting materials

#### 2-2-1- Fabrication from Thallium(I) iodide

The thallium(I) iodide was fabricated through a co-precipitation route  $TlNO_3$  and  $LiI \cdot 2H_2O$  as commencement substances. In the first place, the stoichiometric quantity of  $TlNO_3$  was dissolved in distilled water and the determined quantity of surfactant was affixed to the above mixture. In the end, the solution of  $LiI \cdot 2H_2O$  was added to the above solution to acquire yellow precipitation.

### *2-2-2- Fabrication from Mercury(II) iodide*

The mercury(II) iodide was acquired by combining the  $LiI \cdot 2H_2O$  among a stoichiometry quantity of  $Hg(COOH)_2$  (through examining the coveted molar percentage ratio of  $TlI$  to  $HgI_2$  under several tests). The orange precipitate was obtained by adding  $LiI$  to  $Hg(COOH)_2$  solution.

### *2-2-3- Fabrication from $Tl_4HgI_6$*

The mixture including of  $TlI$  was added into the  $HgI_2$  beaker and stirred at  $25\text{ }^\circ\text{C}$  for 2 h. The orange precipitate was separated, purified utilizing ethanol and distilled water and eventually evaporated into an oven at  $75\text{ }^\circ\text{C}$ . Different conditions was used in sequence to reach the best state. Table 1 clarifies the various states for the fabrication of  $Tl_4HgI_6$ .

### *2-3- Bacterial strains*

The microorganisms applied in this research contained six bacterial varieties, Escherichia coli, Staphylococcus aureus, Pseudomonas aeruginosa, Enterococcus faecalis, Klebsiella pneumonia, Shigella dysenteria and Acinetobacter baumannii.

#### *2-3-1- Determination of the Minimum Inhibitory Concentration (MIC)*

The broth microdilution technique was utilized to survey the minimum inhibitory concentration (MIC) as claimed to the Clinical and Laboratory Standards Institute (CLSI) guidelines [22]. In synopsis, Mueller Hinton broth such as twofold concentration increases of sample 6 was affixed to every well. Mixtures for every bacterium equal to a 0.50 McFarland standard were further thinned and affixed to the plates to reach a specific inoculum of  $10^5 \times 5$  CFU/ml. Then, all the plates were hatched aerobically at  $37\text{ }^\circ\text{C}$  for 18-20 hours. The minimum concentration of the samples that limited the extension of bacteria was recognized as MIC. Besides, MIC measurements were accomplished by Nystatin, Rifampin, and Gentamicin employed as positive inhibitor controls for fungus, Gram-negative, and Gram-positive bacteria.

#### *2-3-2- Determination of the Minimum Bactericidal Concentration (MBC)*

The MBC was estimated by the CLSI guidelines. In synopsis, after the completion of the MIC experiment,  $10\text{ }\mu\text{L}$  from each clean well-including  $Tl_4HgI_6$  was subcultured to Mueller Hinton agar (Becton Dickinson, USA). The plates were incubated at  $37\text{ }^\circ\text{C}$  in air for one day. The colony-forming units (CFU) were determined visually. The MBC was employed as the concentration at which a three-log decrease in

bacterial extension (>99.9%) was identified related to the initial inoculum. Experiments were performed five times.

### *2-3-3- Agar disk diffusion procedure*

Sterilized supplying empty plates soaked with sample 6, and saturated plates (20 µl) were placed on Mueller-Hinton agar plates and incubated at 37°C for 18-20 hours. Bactericidal activities were determined by tracing the cleared area of inhibition to the most near millimeter (mm). Nystatin, Rifampin, and Gentamicin were employed as positive inhibitor controls for fungal, Gram-negative, and Gram-positive bacteria.

### *2-4- Biofilm formation inhibition procedure*

Biofilm production was estimated as specified via Kolter and O'Toole with some adjustments. 100 µl of each  $Tl_4HgI_6$  concentration was affixed to the sterilized 96-well polystyrene microplate. The bacterial culture strains for biofilm assays were provided from the cells were cultured overnight at 37 °C and re-suspended at an optical density at 600 nm (OD600) of 0.2 in 1 ml of tryptic soy broth (TSB). A 100µl of bacterial suspension and 100 µl of each  $Tl_4HgI_6$  concentration are dispersed into every microplate well. Biofilm formation was measured via estimating the biofilm absorption rate of crystal violet (CV) stained biofilm at 570 nm and with entire feasible counts. After one day of the subjection, planktonic cells in microplate wells are removed via rinsing by phosphate-buffered saline (PBS) (pH= 7.2) and dried. Adherent microorganisms were set via combining 200 µl of 96% ethanol for 15 minutes. Next, microplate wells stained by CV (Gram staining set for microscopy-Merck, Germany) stained microplates wells are rinsed twice with PBS to remove CV stain and the microplate were dried at room temperature. To estimate the adherent cell absorbance, the CV was re-solubilized with 200 µl of 33% acetic acid glacial (Merck, Germany) and the absorbance was determined by a microplate reader (ELX-800, Biotec, India) at 570 nm. The biofilm inhibition rates in the attendance of various  $Tl_4HgI_6$  concentrations were measured by using the ratio among the amounts of OD570nm without and with  $Tl_4HgI_6$  [23].

$$\% \text{ inhibition} = \frac{(\text{OD negative control} - \text{OD media control}) - (\text{OD test} - \text{OD nanoparticle control})}{(\text{OD negative control} - \text{OD media control})}$$

## **3- Results And Discussion**

### *3-1- Structural determination*

The X-ray diffraction patterns of specimens 3, 5, and 6 are demonstrated in Figure 1 (a-c). As shown in Figure 1a, a product was achieved with high purity and good crystallinity when the mole ratio of  $TlI$  :  $HgI_2$  was chosen 4:1. This pattern indicates that the diffraction peaks are in the match with the reference code number of pure  $Tl_4HgI_6$  71-1852, possessing a tetragonal structure with a lattice constant of the unit cell:  $c = 9.260$ , and  $a = b = 9.446$ . So, the optimum ratio was 4:1 and adjusted for the other experiments. A

simple phase of  $Tl_4HgI_6$  nano-structures was fabricated among tetragonal structure (reference code: 71-1852) by using SDS as an anionic surfactant (Figure 1b). Figure 1c illustrates XRD pattern of  $Tl_4HgI_6$  nanostructures in attendance of polymeric surfactant (PVP-25000). This pattern indicates that all of the diffractions conform, including the pure  $Tl_4HgI_6$  (reference code: 71-1852), possessing a tetragonal structure amidst the lattice constant of the unit cell:  $c = 9.260$ ,  $a = b = 9.446$ . The crystallite size was estimated by Scherrer equation,  $D_g = K\lambda/\beta\cos\theta$ ,  $\theta$  is the Bragg angle,  $\lambda$  is the wavelength of X-ray,  $K$  is a non-dimensional shape factor, which usually is nearly 0.9, and  $\beta$  is the region of the detected diffraction line on its half intensity maximum [24]. The grain sizes of the specimens are in the extent of 20-37 nm.

### *3-2- Structure and size characterization*

In the current paper, diverse factors were changed to obtain the tiniest specimen amidst high uniformity and the influence of them was investigated on structure, size and shape of specimens via the FESEM images. Figure 2 illustrates the SEM images of as-fabricated  $Tl_4HgI_6$  by changing the molarity of  $TlI$  and  $HgI_2$ . As shown in Figure 2a, the micro-structures were produced when the mole ratio of  $TlI$  to  $HgI_2$  was 1: 1 (specimen 1). Figure 2b presents the FESEM images of specimen 2 that was composed in 2: 1 mole ratio of  $TlI$  to  $HgI_2$ . The microstructures were fabricated the same as specimen 1. The nanoparticles with highly alike and similar size particles was formed in specimen 3, when the mole ratio was 4: 1 (Figure 2c). The uniformity in specimen 3 is fairly high and the average of particle size is about 44 nm. The microstructures were fabricated, when the mole ratio of  $TlI$  to  $HgI_2$  was 1: 2 and the morphology is heterogeneous (Figure 2d). Therefore, the optimum mole ratio between  $TlI$  :  $HgI_2$  was chosen 4:1. This mole ratio was utilized to explore the influence of the different surfactants on the structure, shape, and size of the specimens. Figure 2(e-i) illustrates the FESEM images of the specimens in the existence of different surfactant. As revealed in Figure 2e, in presence of SDS, the product was made of nanostructures and the average size of nanoparticle is about 19 nm. The uniform nanoparticles with the mean size of 74 nm were composed by applying PVP as a polymeric surfactant (Figure 2f). By utilizing EDTA, the morphology of the product is heterogeneous micro-particles (Figure 2g). In the presence of NaHSal the FESEM images of the product displays bulk structures with some nanoparticles. (Figure 2h). As shown in Figure 2i, in the presence of HTAB, the product made from cubic particles with tiny nanoparticles and the average size of particles is around 22 nm. Figure 2(j-l) illustrates the EDX spectra of  $Tl_4HgI_6$  nanostructures (samples 3, 5, and 6, respectively). In these spectrums, the peaks of  $Tl$ ,  $Hg$ , and  $I$  elements can be noticed. The results show that the purity of the products is high.

Figure 3(a-d) reveals the histograms of the particle diameters of samples 3, 5, 6 and 9 estimated of its FESEM images employing Digimizer program, respectively. Figure 3a shows that 46 % of sample 3 has a size particle between 30-50 nm. 50 % of Sample 5 possesses the size distribution between 10-20 nm. The histograms of particle size of specimen 6 is demonstrated in Figure 3c. As shown in this Figure 44% of particles are between 70-90 nm.

Figure 4(a-b) demonstrates TEM images of the optimum product (specimen 6). As-prepared  $\text{Tl}_4\text{HgI}_6$  in multiple scales 20 and 150 nm, sequentially. The average particle size from nano- $\text{Tl}_4\text{HgI}_6$  was estimated at 35 nm, which is in almost correct compromise by the FESEM and XRD results. Figure 4c indicates the HRTEM of specimen 6. The crystalline planes were identified by the parallel lines indicate the high degree of crystallinity of the compound. The lattice fringes are clearly shown with spacing fringes of 2.95 Å, which well-matched with the crystal planes (212) of  $\text{Tl}_4\text{HgI}_6$  crystals. This image shows spherical particles having spherical cross-sections. Besides, it shows that the particles in the FESEM image consist of several spheres.

### 3-3- Raman spectroscopy

Figure 5a reveals the Raman spectra at ambient temperature (25 °C) from nano- $\text{Tl}_4\text{HgI}_6$  (specimen 3). The specific absorptions of nano- $\text{Tl}_4\text{HgI}_6$  indicated within the extent from 30-250  $\text{cm}^{-1}$ . Six absorption peaks can be perceived in this spectra, which were situated at 36.5, 42.5, 57.4, 66.3, 75.2, and 172.1  $\text{cm}^{-1}$ . All six bands are in accordance to  $\text{Tl}_4\text{HgI}_6$  [25]. Likewise the bands at 57.4 and 66.3  $\text{cm}^{-1}$  are allocated to the symmetric stretching of the TI-I [26]. Raman movement rates of nano- $\text{Tl}_4\text{HgI}_6$  was correlated to the Raman movement rates of  $\text{Tl}_4\text{HgI}_6$  detailed in the reports. The outcomes offer a blue movement within the Raman spectra due to the stress and the captivity of phonon impact which made up through decreasing the particle size [27, 28]. Figure 5b indicates the Raman spectra at (25 °C) from the specimen 6. The specific absorptions of nano- $\text{Tl}_4\text{HgI}_6$  were indicated within the extent from 30-250  $\text{cm}^{-1}$ . Six absorption peaks can see at 36.5, 42.5, 51.4, 69.3, 104.8, and 178.0  $\text{cm}^{-1}$ . All six bands are in accordance to  $\text{Tl}_4\text{HgI}_6$  [26]. Also, the bands at 51.4  $\text{cm}^{-1}$  and 69.3  $\text{cm}^{-1}$  were attributed to the symmetrical stretching of the TI-I [26]. Raman movement rates of nano- $\text{Tl}_4\text{HgI}_6$  were correlated to Raman movement rates of  $\text{Tl}_4\text{HgI}_6$  detailed in the reports [27]. The outcomes offer a blue movement within the Raman spectra due to the stress and the captivity of phonon impact which made up through decreasing the particle size [28].

### 3-4- Antibacterial activity

#### 3-4-1- Determination of MIC

The MICs and MBC were assessed via the broth microdilution technique and the outcomes are displayed in Table 2. The MIC of  $\text{Tl}_4\text{HgI}_6$  was estimated by the lowest concentration factor that ultimately inhibits visible growth. As shown in Table 2, MIC utilized values have been varied from 31.5 to 61.26  $\mu\text{g/ml}$ . The attained values for  $\text{Tl}_4\text{HgI}_6$  were 31.5  $\mu\text{g/ml}$  against *S. aureus*, *E. coli* and *M. catarrhalis* and 62.5  $\mu\text{g/ml}$  against *E. faecalis*, *P. aeruginosa*, *K. pneumonia*, and *S. dysenteriae*. Despite that, none inhibitory efficacy was noticed on *A. baumannii*. The results revealed that the maximum antibacterial activity of  $\text{Tl}_4\text{HgI}_6$  was perceived against *S. aureus*, *E. coli* and *M. catarrhalis*. These outcomes demonstrate that  $\text{Tl}_4\text{HgI}_6$  displays efficient antibacterial activity against Gram-positive and Gram-negative bacteria.

#### 3-4-2- Agar disk-diffusion

Disk diffusion was determined by evaluating the growth inhibition zone diameters on the examined microorganisms. The inhibition zone diameter in the disk is provided in millimeters. The experiments were reiterated three times, and the outcomes are exhibited in Table 3 and Figure 6. It can be observed from the table that *E. feacalis* have higher inhibition growth zone than other examined bacteria.  $Tl_4Hgl_6$  reveals remarkable antibacterial activity the inhibition zone was extremely clear, including larger diameters of 24 mm and 22 mm for bacterial media, including *E. feacalis*, *E. coli*, and *S. aureus*, respectively.

### 3-4-3- Biofilm formation inhibition

The effect of  $Tl_4Hgl_6$  nanoparticles on biofilm production was examined with *S.aureus* and *E.feacalis*, as strong biofilm creator. As presented in Figure 7 the achieved result was depended on the concentration. The best reduction of biofilm was recognized in higher  $Tl_4Hgl_6$  concentrations ( $2\times MIC$ ).  $Tl_4Hgl_6$  at  $2\times MIC$  concentration inhibits biofilm production by *S. aureus* and *E. feacalis* with an inhibition percentage of 95% and 90%, respectively. The biofilm growth inhibition at the  $Tl_4Hgl_6$  concentration higher than MIC confirmed that the bacterial cells in a biofilm are more persistent to antibacterial factors correlated to the planktonic cells, which is a renowned characteristic.

## 4- Conclusions

In summary, the co-precipitation technique was adopted to fabricate nano- $Tl_4Hgl_6$  for the first time. Several factors were developed to obtain tiny specimens and pure phase. The mole percentage ratio of  $TlI$  to  $Hgl_2$  and the variety of surfactant can influence the particle size and purity. The function of surfactants on the particle size of the specimens was confirmed via the XRD patterns and FESEM images. The results obviously showed that the homogenous structure was produced in the presence of PVP-25000. The antibacterial and anti-biofilm activities of  $Tl_4Hgl_6$  revealed that the maximum antibacterial activity of  $Tl_4Hgl_6$  was perceived against *S. aureus*, *E.coli* and *M. catarils*. These outcomes demonstrate that  $Tl_4Hgl_6$  displays efficient antibacterial activity against Gram-positive and Gram-negative bacteria. The best biofilm decrease was recognized in higher  $Tl_4Hgl_6$  concentrations ( $2\times MIC$ ).  $Tl_4Hgl_6$  at  $2\times MIC$  concentration inhibits biofilm production by *S. aureus* and *E. feacalis* with an inhibition percentage of 95% and 90%, respectively.

## Declarations

### Ethics approval and consent to participate

Not applicable.

### Consent for publication

Not applicable.

### Availability of data and materials

All data generated or analysed during this study are included in this published article.

### **Competing interests**

The authors declare that they have no competing interests.

### **Funding**

Not applicable.

### **Authors' contributions**

MK: Software, Investigation, Formal analysis. MG: Visualization, Formal analysis, Writing -review & editing, Investigation. OA: Data curation, Resources, Validation. MSN: Conceptualization, Methodology, Supervision, Project administration, Data curation, Resources, Validation. SR: Investigation, Formal analysis.

All authors analyzed and interpreted the results.

### **Acknowledgements**

Authors are grateful to the council of Iran National Science Foundation (97017837) and University of Kashan for supporting this work by Grant No (159271/10).

## **References**

- [1] Prestinaci F, Pezzotti P, Pantosti A. Antimicrobial resistance: a global multifaceted phenomenon. *Pathogens and global health* 2015;109:309-18.
- [2] Savage VJ, Chopra I, O'Neill AJ. Staphylococcus aureus biofilms promote horizontal transfer of antibiotic resistance. *Antimicrobial agents and chemotherapy* 2013;57:1968-70.
- [3] Huseby DL, Brandis G, Alzrigat LP, Hughes D. Antibiotic resistance by high-level intrinsic suppression of a frameshift mutation in an essential gene. *Proceedings of the National Academy of Sciences* 2020;117:3185-91.
- [4] Arciola CR, Campoccia D, Speziale P, Montanaro L, Costerton JW. Biofilm formation in Staphylococcus implant infections. A review of molecular mechanisms and implications for biofilm-resistant materials. *Biomaterials* 2012;33:5967-82.
- [5] Stalder T, Cornwell B, Lacroix J, Kohler B, Dixon S, Yano H, et al. Evolving populations in biofilms contain more persistent plasmids. *Molecular biology and evolution* 2020;37:1563-76.
- [6] Olsen I. Biofilm-specific antibiotic tolerance and resistance. *European Journal of Clinical Microbiology & Infectious Diseases* 2015;34:877-86.

- [7] Buhmann MT, Stiefel P, Maniura-Weber K, Ren Q. In vitro biofilm models for device-related infections. *Trends in Biotechnology* 2016;34:945-8.
- [8] Koch G, Yepes A, Förstner KU, Wermser C, Stengel ST, Modamio J, et al. Evolution of resistance to a last-resort antibiotic in *Staphylococcus aureus* via bacterial competition. *Cell* 2014;158:1060-71.
- [9] Djoko KY, Goytia MM, Donnelly PS, Schembri MA, Shafer WM, McEwan AG. Copper (II)-bis (thiosemicarbazonato) complexes as antibacterial agents: insights into their mode of action and potential as therapeutics. *Antimicrobial agents and chemotherapy* 2015;59:6444-53.
- [10] Ghosh C, Haldar J. Membrane-active small molecules: designs inspired by antimicrobial peptides. *ChemMedChem* 2015;10:1606-24.
- [11] Pani R, Pellegrini R, Cinti M, Bennati P, Betti M, Vittorini F, et al.  $\text{LaBr}_3$ : Ce crystal: The latest advance for scintillation cameras. *Nuclear Instruments and Methods in Physics Research Section A: Accelerators, Spectrometers, Detectors and Associated Equipment* 2007;572:268-9.
- [12] Zandbergen H. The crystal structure of  $\alpha$ -thallium hexaiodochromate,  $\alpha\text{-Tl}_4\text{CrI}_6$ . *Acta Crystallographica Section B: Structural Crystallography and Crystal Chemistry* 1979;35:2852-5.
- [13] Ghanbari M, Salavati-Niasari M.  $\text{Tl}_4\text{CdI}_6$  nanostructures: facile sonochemical synthesis and photocatalytic activity for removal of organic dyes. *Inorganic chemistry* 2018;57:11443-55.
- [14] Singh N, Suhre D, Green K, Fernelius N, Hopkins F. Ternary halides: novel NLO compounds for LWIR. *Operational Characteristics and Crystal Growth of Nonlinear Optical Materials II: International Society for Optics and Photonics*; 2005. p. 591203.
- [15] Nair SM, Yahya A, Ahmad A. Ionic conductivity and dielectric constant of  $\text{Tl}_4\text{CdI}_6$ . *Solid state ionics* 1996;86:137-9.
- [16] Avdienko K, Badikov D, Badikov V, Chizhikov V, Panyutin V, Shevyrdyaeva G, et al. Optical properties of thallium mercury iodide. *Optical Materials* 2003;23:569-73.
- [17] Hagemann M, Weber H-J. Are ternary halides useful materials for nonlinear optical applications? *Applied physics A* 1996;63:67-74.
- [18] Parasyuk O, Khyzhun O, Piasecki M, Kityk I, Lakshminarayana G, Luzhnyi I, et al. Synthesis, structural, X-ray photoelectron spectroscopy (XPS) studies and IR induced anisotropy of  $\text{Tl}_4\text{HgI}_6$  single crystals. *Materials Chemistry and Physics* 2017;187:156-63.
- [19] Kalyagin D, Ermolenko YE, Vlasov YG. Diffusion of Tl-204 isotope and ionic conductivity in  $\text{Tl}_4\text{HgI}_6$  membrane material for chemical sensors. *Russian Journal of Applied Chemistry* 2008;81:2172-4.

- [20] Ermolenko YE, Kalyagin D, Subbotina S, Kolodnikov V, Vlasov YG. Thallium-selective sensor with a membrane based on  $Tl_4HgI_6$  ionic conductor. *Russian Journal of Applied Chemistry* 2013;86:192-9.
- [21] Gholamrezaei S, Ghanbari M, Amiri O, Salavati-Niasari M, Foong LK.  $BaMnO_3$  nanostructures: Simple ultrasonic fabrication and novel catalytic agent toward oxygen evolution of water splitting reaction. *Ultrasonics sonochemistry* 2020;61:104829.
- [22] Vijayakumar S, Malaikozhundan B, Parthasarathy A, Saravanakumar K, Wang M-H, Vaseeharan B. Nano Biomedical Potential of Biopolymer Chitosan-Capped Silver Nanoparticles with Special Reference to Antibacterial, Antibiofilm, Anticoagulant and Wound Dressing Material. *Journal of Cluster Science* 2020;31:355-66.
- [23] Murthy PS, Venugopalan V, Arunya DD, Dhara S, Pandiyan R, Tyagi A. Antibiofilm activity of nano sized CuO. *International Conference on Nanoscience, Engineering and Technology (ICONSET 2011): IEEE;* 2011. p. 580-3.
- [24] Orooji Y, Ghanbari M, Amiri O, Salavati-Niasari M. Facile fabrication of silver iodide/graphitic carbon nitride nanocomposites by notable photo-catalytic performance through sunlight and antimicrobial activity. *Journal of Hazardous Materials* 2020;389:122079.
- [25] Yukhymchuk VO, Dzhagan VM, Mazur NV, Parasyuk OV, Khyzhun OY, Luzhnyi IV, et al. Experimental and theoretical study of Raman scattering spectra of ternary chalcogenides  $Tl_4HgI_6$ ,  $Tl_4HgBr_6$ , and  $TlHgCl_3$ . *JRSp* 2018;49:1840-8.
- [26] Brafman O, Mitra S, Crawford R, Daniels W, Postmus C, Ferraro J. Pressure dependence of Raman spectra of solids. Phase transition in TII. *Solid State Communications* 1969;7:449-52.
- [27] Xu C, Zhang P, Yan L. Blue shift of Raman peak from coated  $TiO_2$  nanoparticles. *Journal of Raman spectroscopy* 2001;32:862-5.
- [28] Ammlung R, Shriver D, Kamimoto M, Whitmore D. Conductivity and Raman spectroscopy of new indium (I) and thallium (I) ionic conductors.  $In_4CdI_6$ ,  $In_2ZnI_4$ , and  $Tl_2ZnI_4$ , and the related compound  $Tl_4CdI_6$ . *Journal of Solid State Chemistry* 1977;21:185-93.

## Tables

**Table 1** Preparation conditions for  $Tl_4HgI_6$

Specimen no.	TII : Hgl <sub>2</sub> molar ratio	Type of capping agent	Products
1	1	-	Tl <sub>4</sub> Hgl <sub>6</sub> , Hgl <sub>2</sub>
2	2	-	Tl <sub>4</sub> Hgl <sub>6</sub> , Hgl <sub>2</sub>
3	4	-	Tl <sub>4</sub> Hgl <sub>6</sub>
4	0.5	-	Hgl <sub>2</sub>
5	4	SDS	Tl <sub>4</sub> Hgl <sub>6</sub> , Tl <sub>2</sub> Hgl <sub>4</sub>
6	4	PVP	Tl <sub>4</sub> Hgl <sub>6</sub>
7	4	EDTA	Tl <sub>4</sub> Hgl <sub>6</sub> , TII
8	4	NaHSal	Tl <sub>4</sub> Hgl <sub>6</sub>
9	4	HTAB	TII

**Table 2** The mean Minimum Inhibitory Concentration (MIC) and Minimal Bactericidal Concentration (MBC) of Tl<sub>4</sub>Hgl<sub>6</sub> against tested microorganisms.

Microorganisms	MIC(µg/ml)	MBC(µg/ml)
<i>Staphylococcus aureus</i>	31.25	125
<i>Enterococcus faecalis</i>	62.5	250
<i>Pseudomonas aeruginosa</i>	62.5	250
<i>Escherichia coli</i>	31.25	250
<i>Acinetobacter baumannii</i>	-	-
<i>Moraxella cataralis</i>	31.25	31.25
<i>Klebsiella pneumonia</i>	62.5	500
<i>Shigella dysenteriae</i>	62.5	62.5

**Table 3** The mean inhibition zones (mm) of Tl<sub>4</sub>Hgl<sub>6</sub> against tested microorganism

Microorganisms	Diameters of zones of growth inhibition (mm)
<i>Staphylococcus aureus</i>	22
<i>Enterococcus faecalis</i>	24
<i>Pseudomonas aeruginosa</i>	11
<i>Escherichia coli</i>	22
<i>Acinetobacter baumannii</i>	-
<i>Klebsiella pneumonia</i>	17
<i>Shigella dysenteriae</i>	18

## Figures

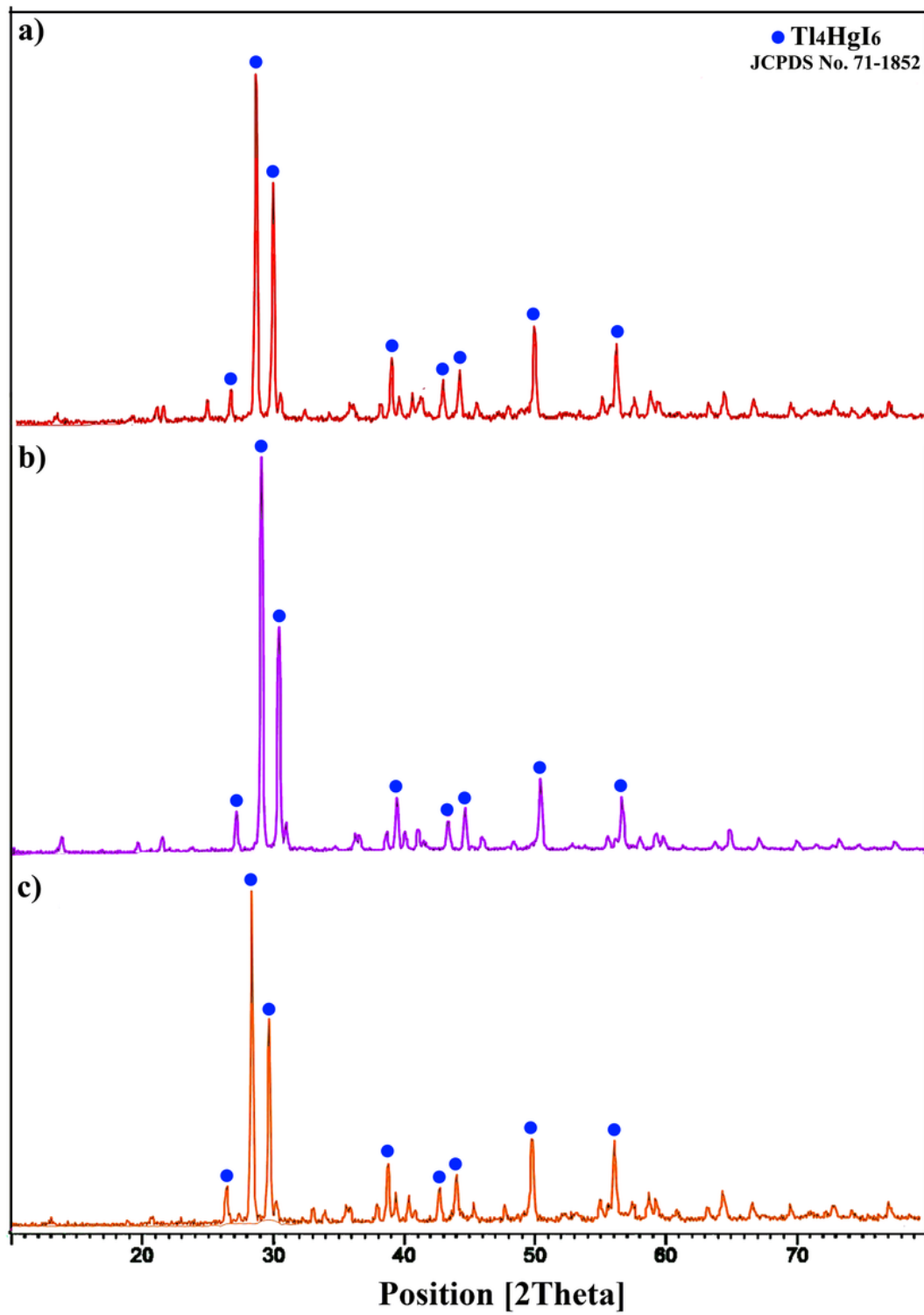


Figure 1

XRD pattern of specimens (a) 3, (b) 5, and (c) 6.

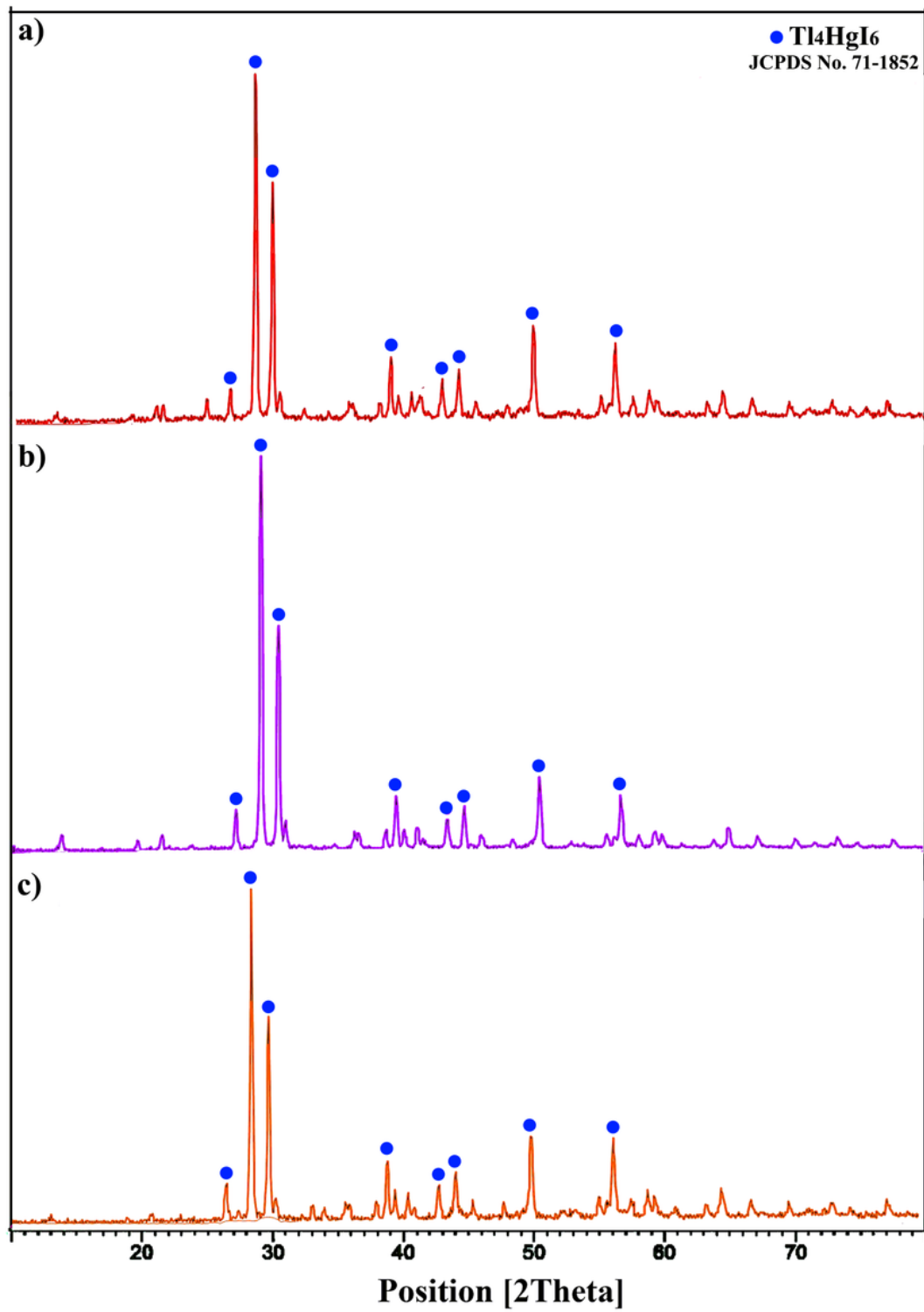
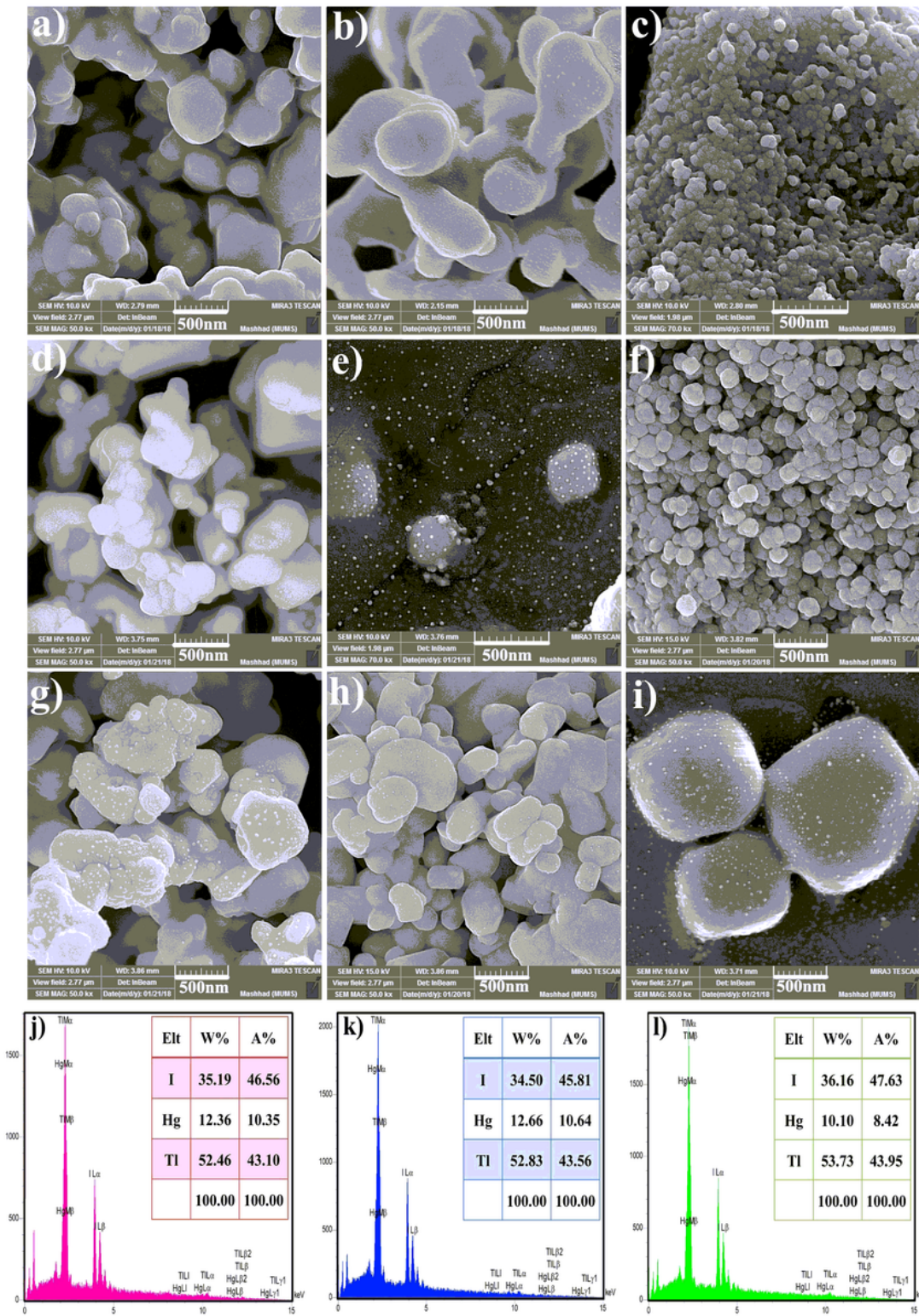


Figure 1

XRD pattern of specimens (a) 3, (b) 5, and (c) 6.



**Figure 2**

FESEM images of the specimens (a) 1, (b) 2, (c) 3, (d) 4, (e) 5, (f) 6, (g) 7, (h) 8, (i) 9, EDX spectrum of the specimens (j) 2, (k) 3, (l) 5.

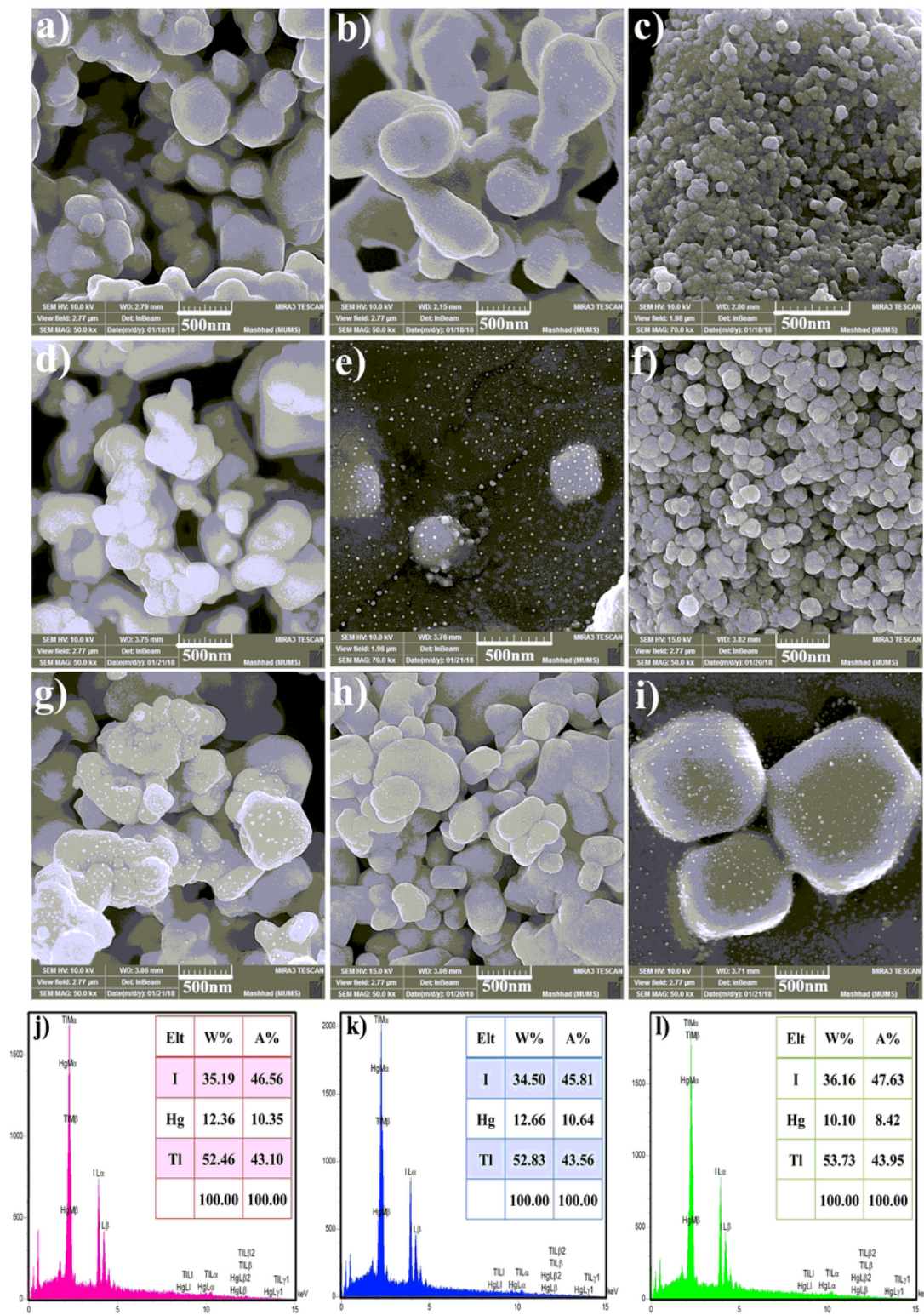


**Figure 2**

FESEM images of the specimens (a) 1, (b) 2, (c) 3, (d) 4, (e) 5, (f) 6, (g) 7, (h) 8, (i) 9, EDX spectrum of the specimens (j) 2, (k) 3, (l) 5.

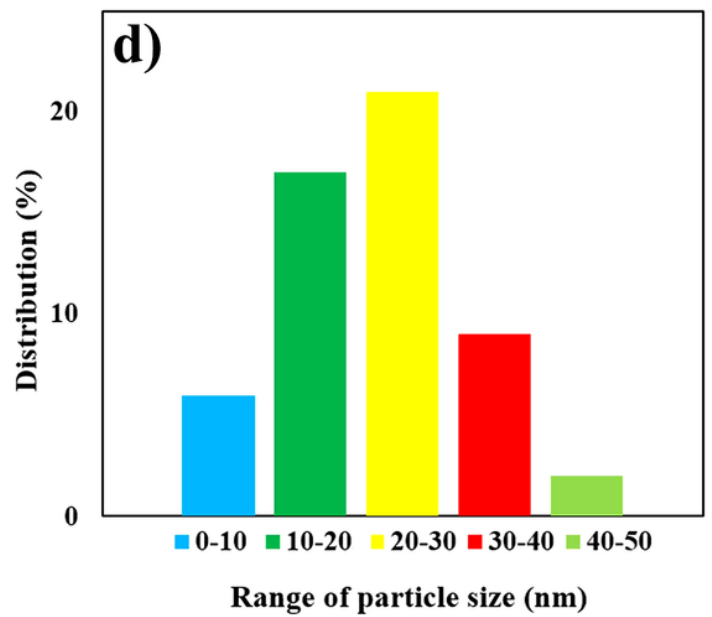
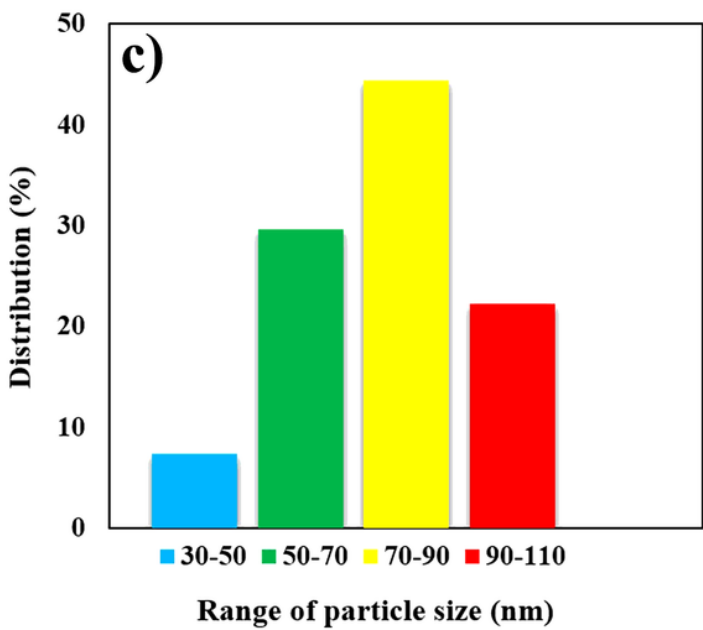
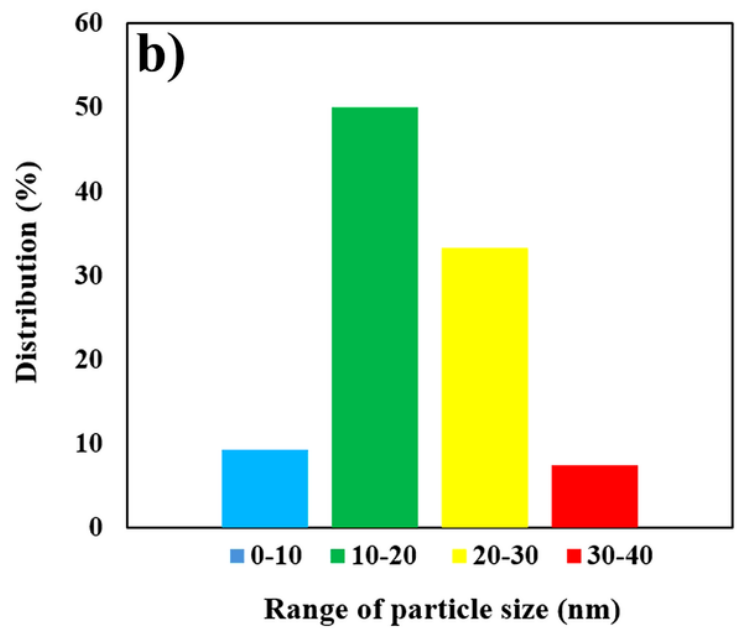
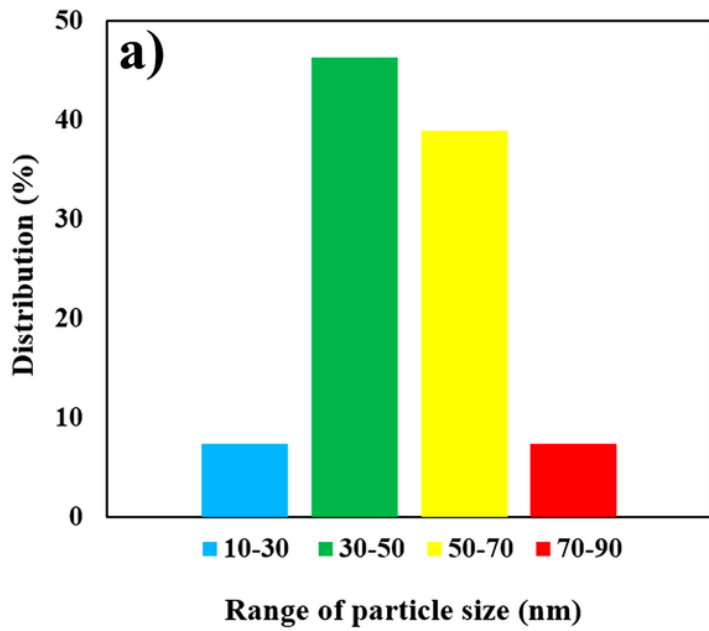


**Figure 3**

The particle size distribution of the specimens a) 3, b) 5, c) 6 and d) 9.

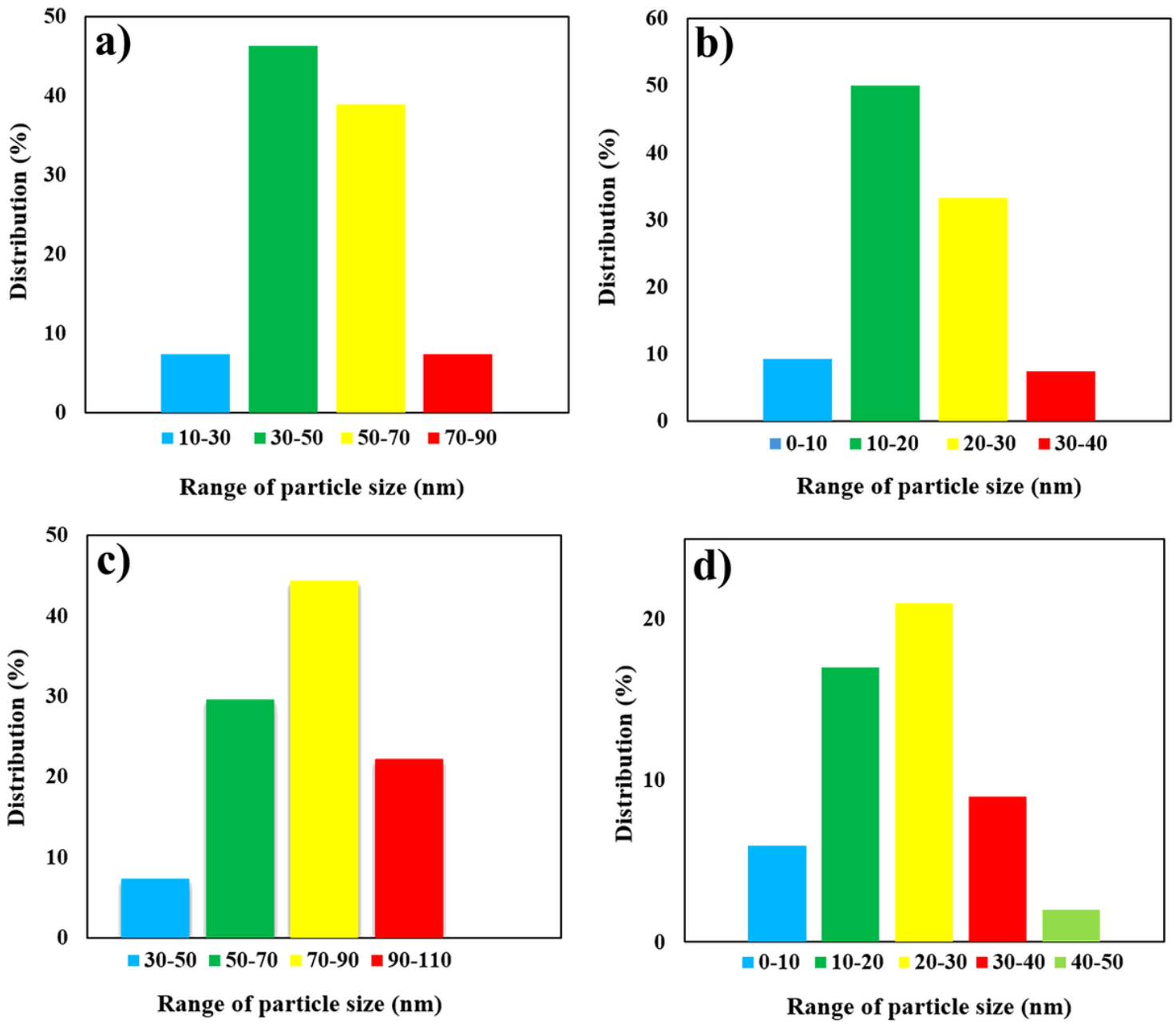


**Figure 3**

The particle size distribution of the specimens a) 3, b) 5, c) 6 and d) 9.

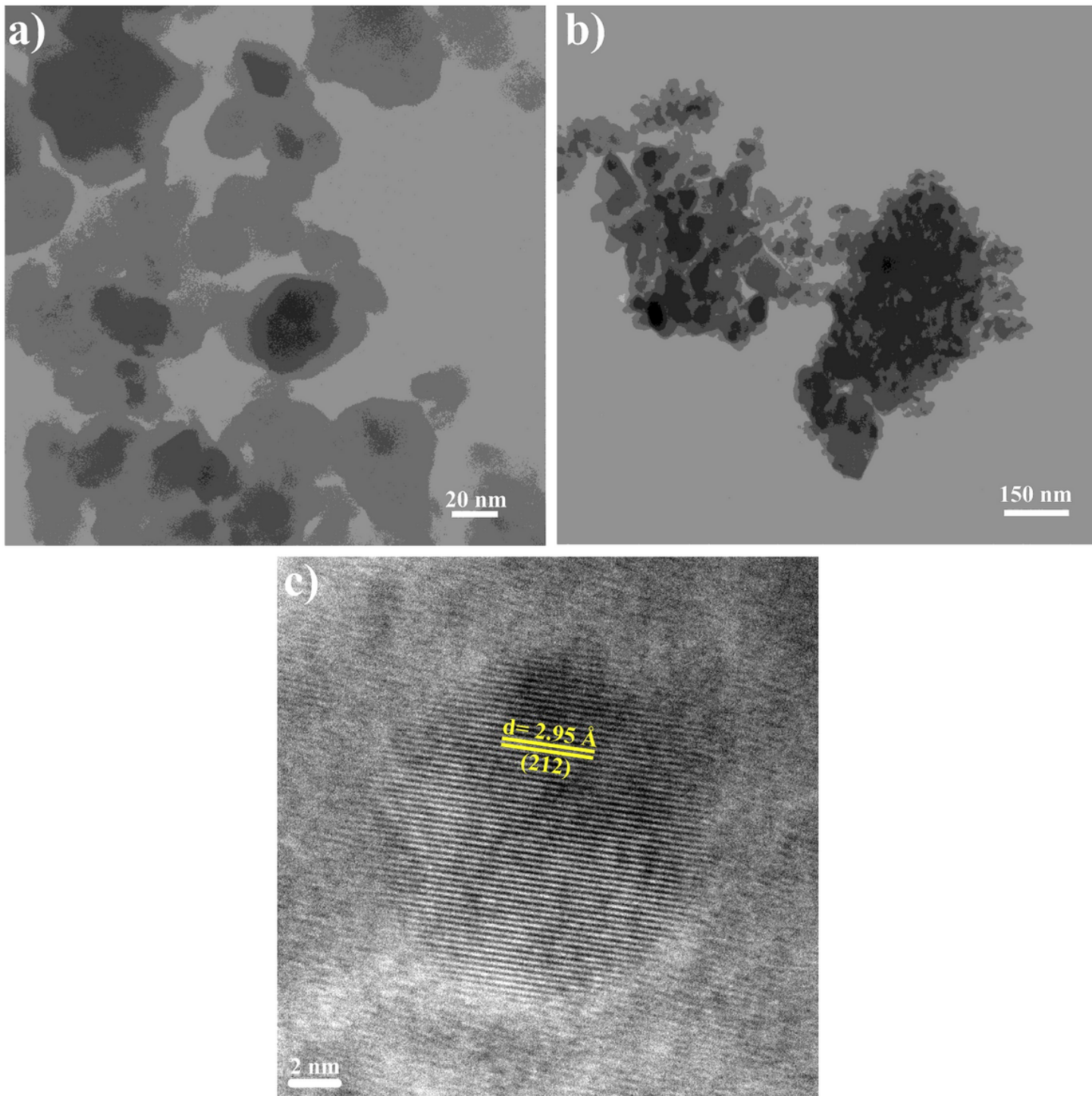


**Figure 4**

(a-b) TEM and c) HRTEM images of the specimen 6.

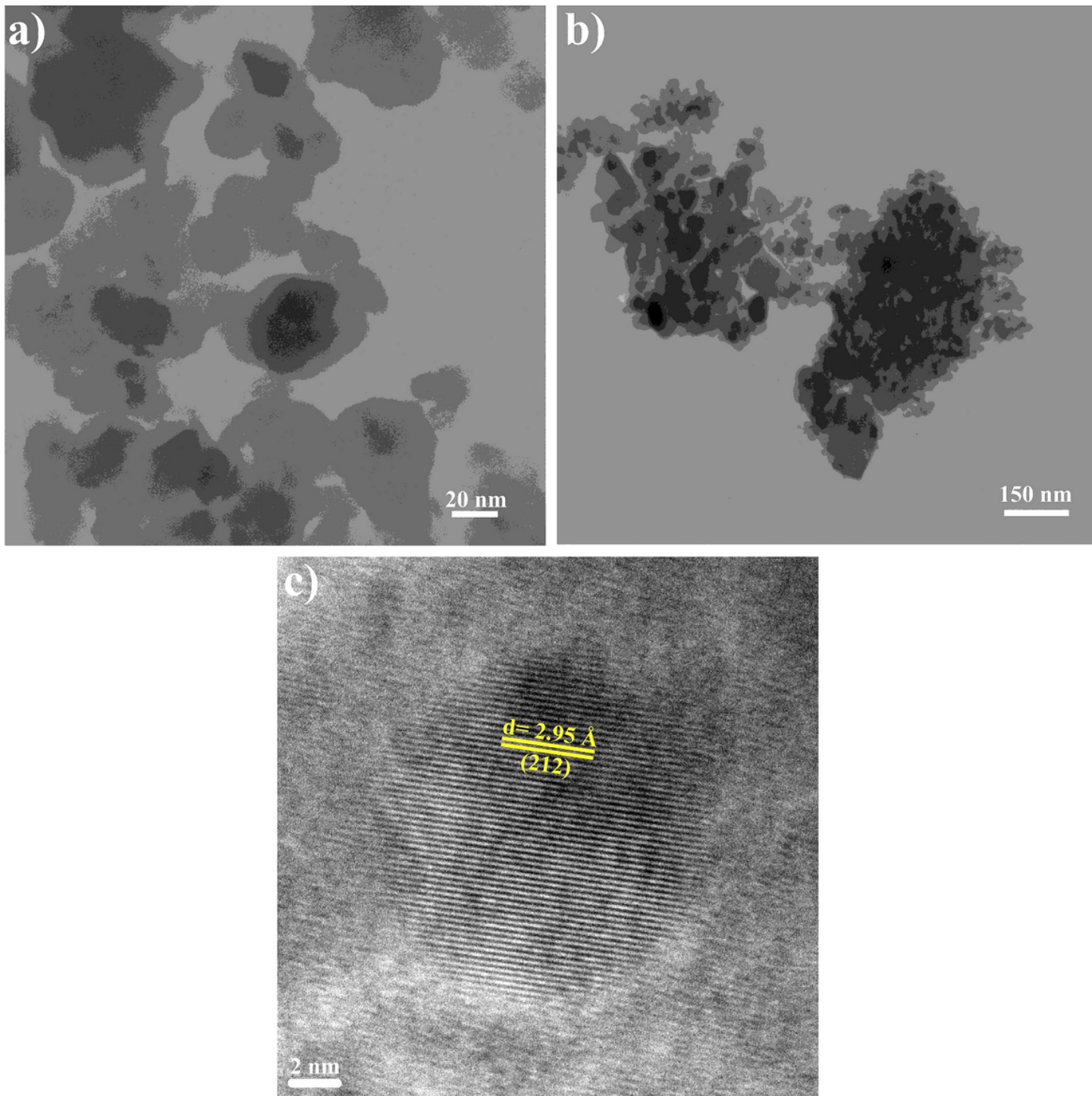


**Figure 4**

(a-b) TEM and c) HRTEM images of the specimen 6.

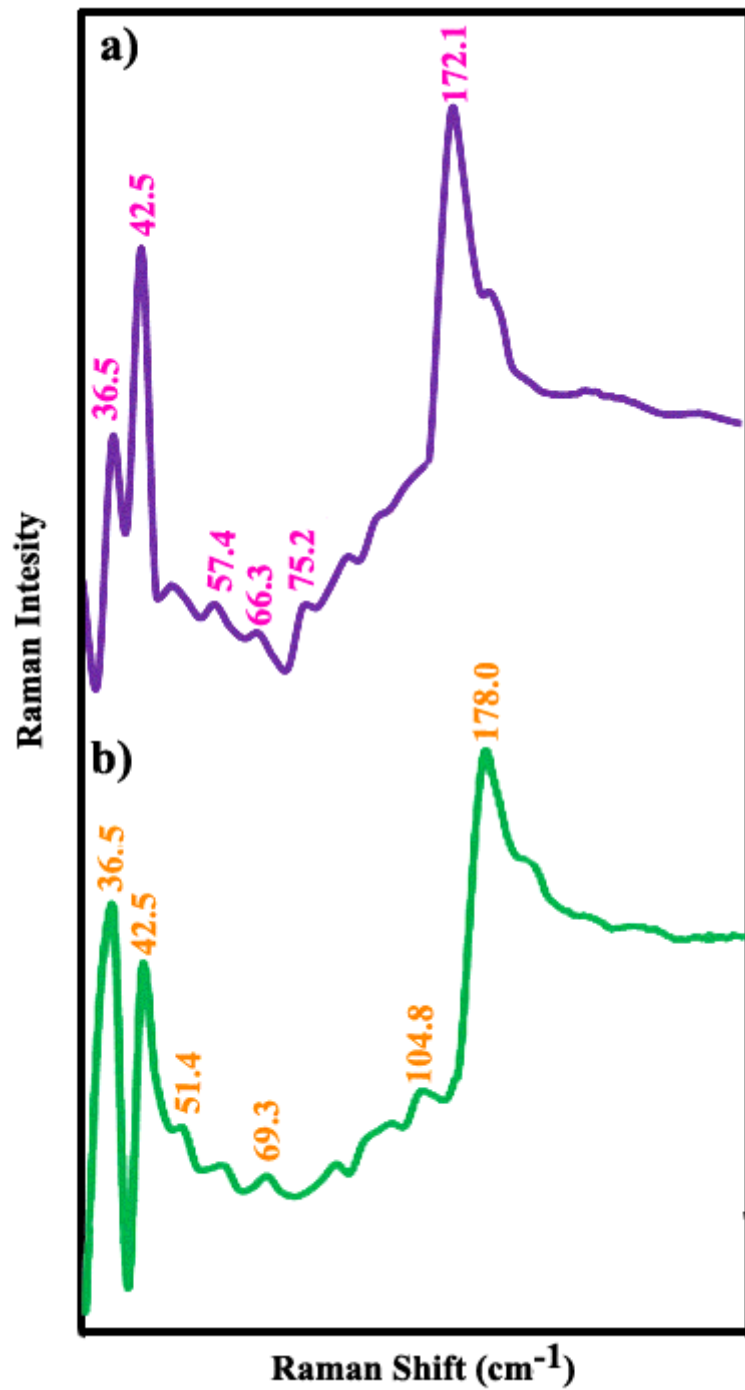


Figure 5

Raman spectra of the specimens (a) 3 and (b) 6.

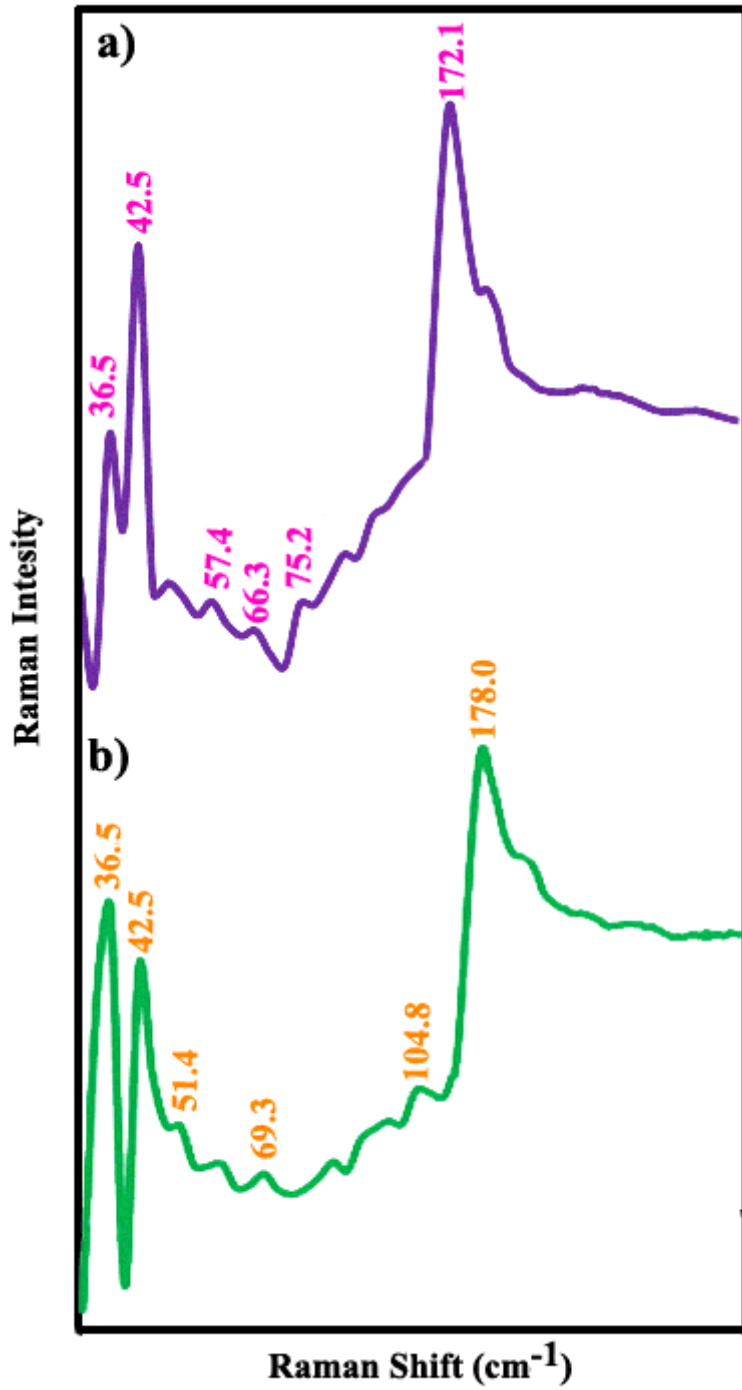
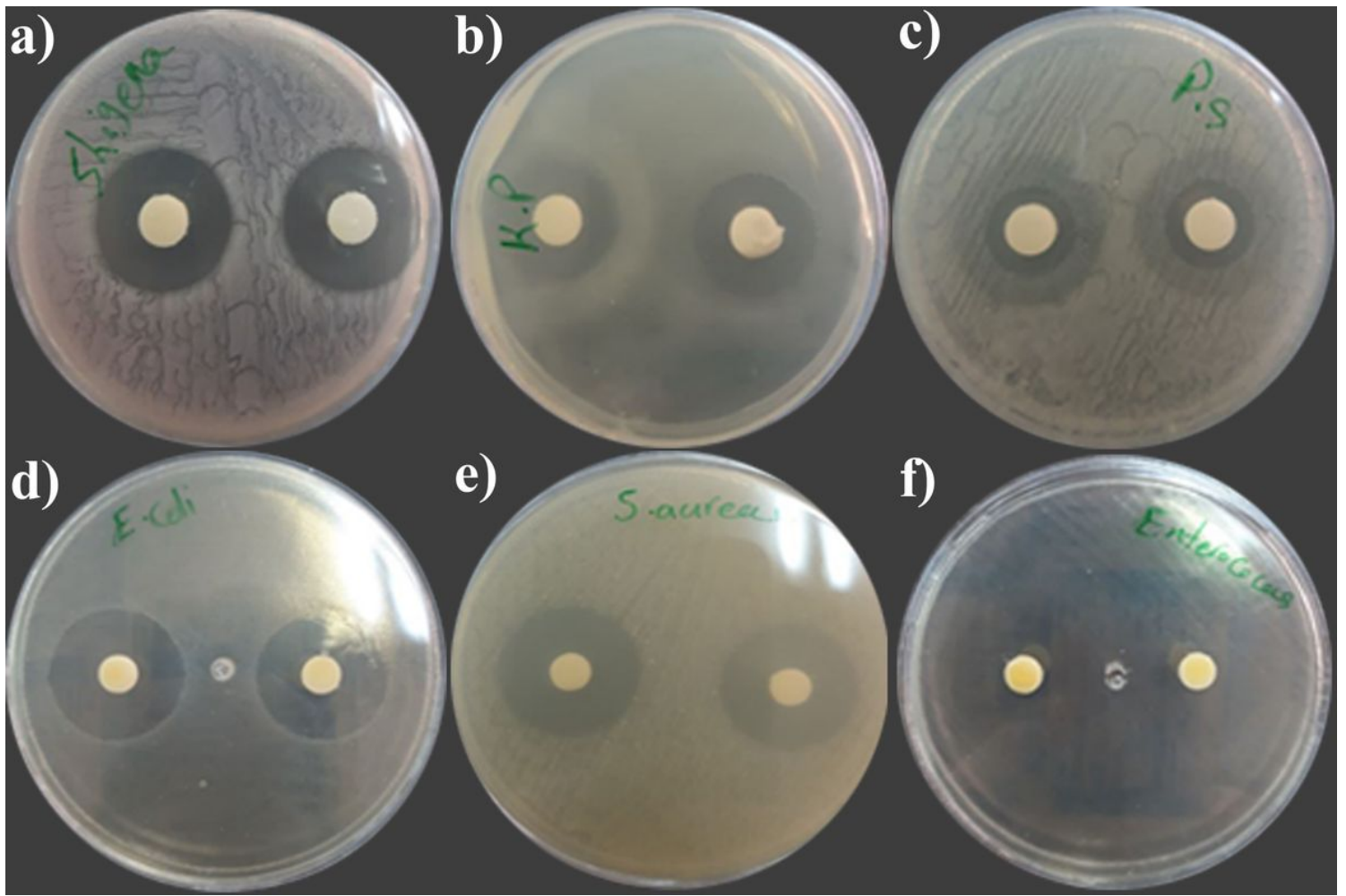


Figure 5

Raman spectra of the specimens (a) 3 and (b) 6.



**Figure 6**

Inhibition zones of T14Hgl6 against a) *Sh. Dysenteriae*, b) *K. pneumoniae*, c) *P. aeruginosa*, d) *E. coli*, e) *S. aureus*, and f) *E. faecalis*.

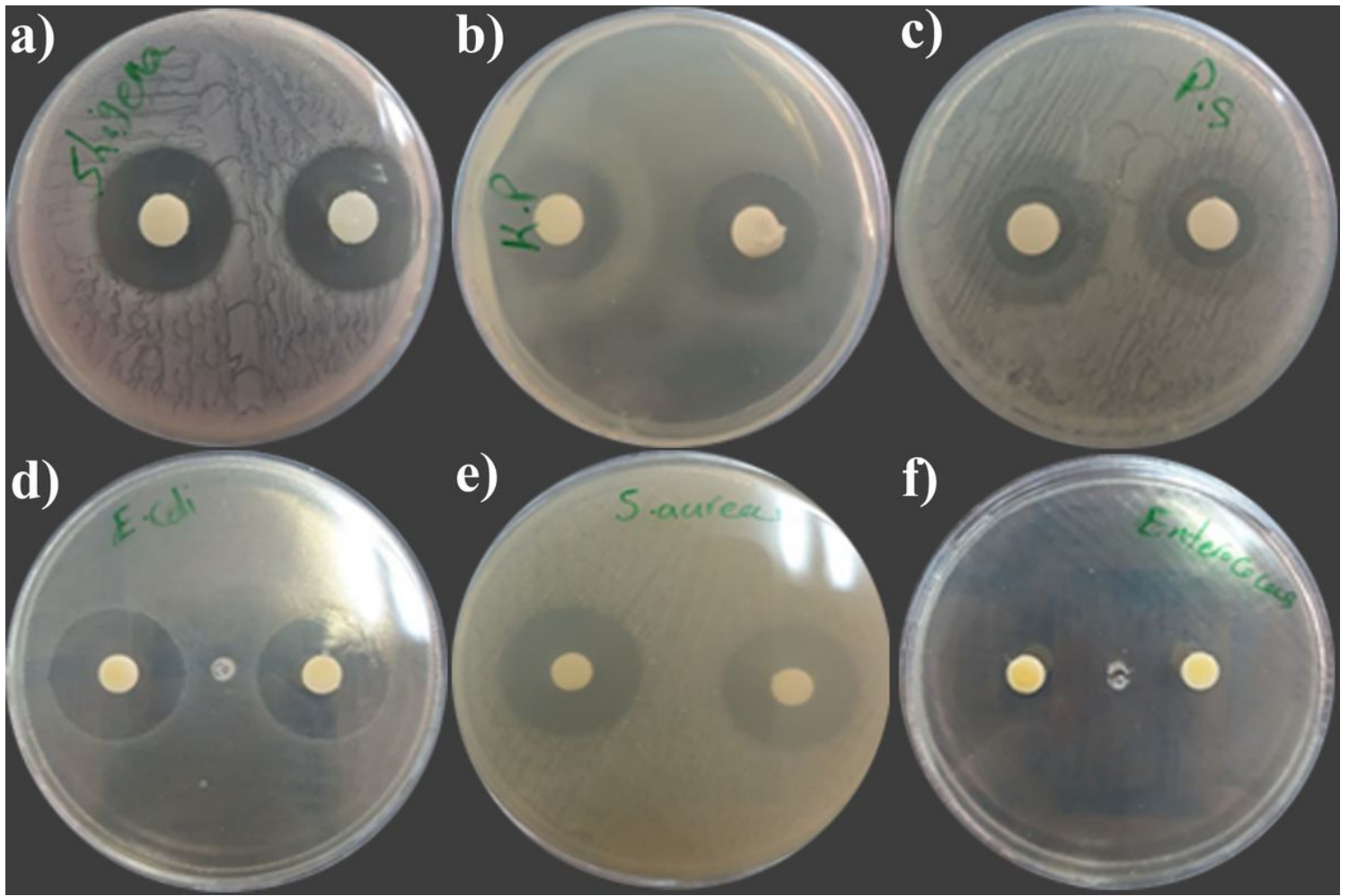


**Figure 6**

Inhibition zones of T14Hgl6 against a) *Sh. Dysenteriae*, b) *K. pneumonia*, c) *P. aeruginosa*, d) *E.coli*, e) *S.aureus*, and f) *E.feacalis*.

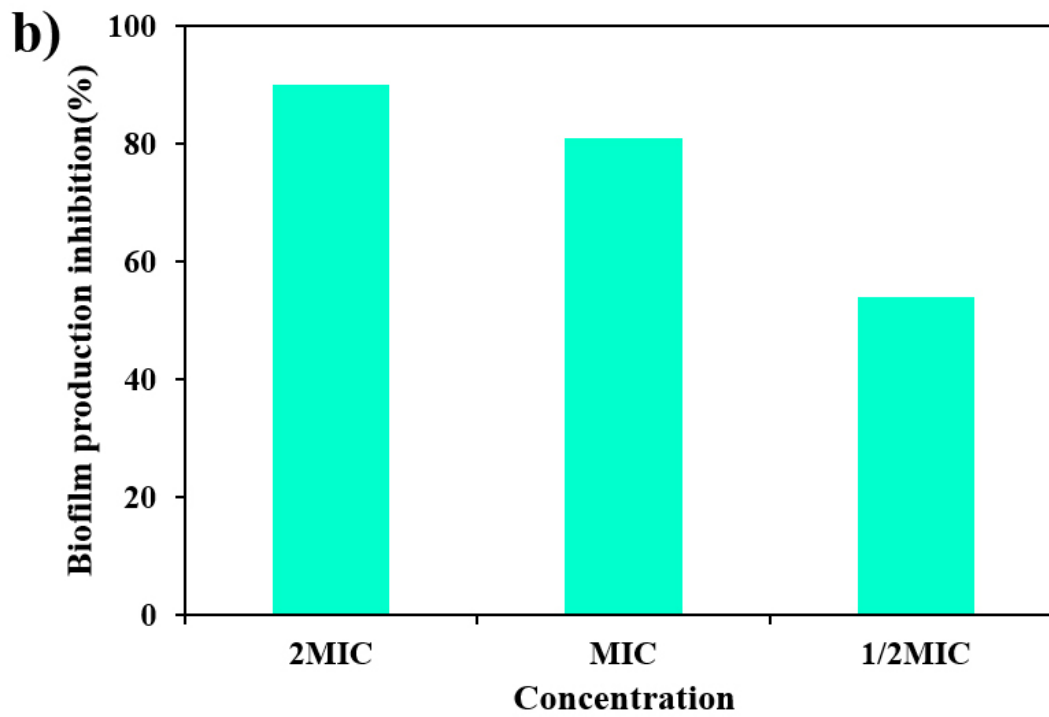
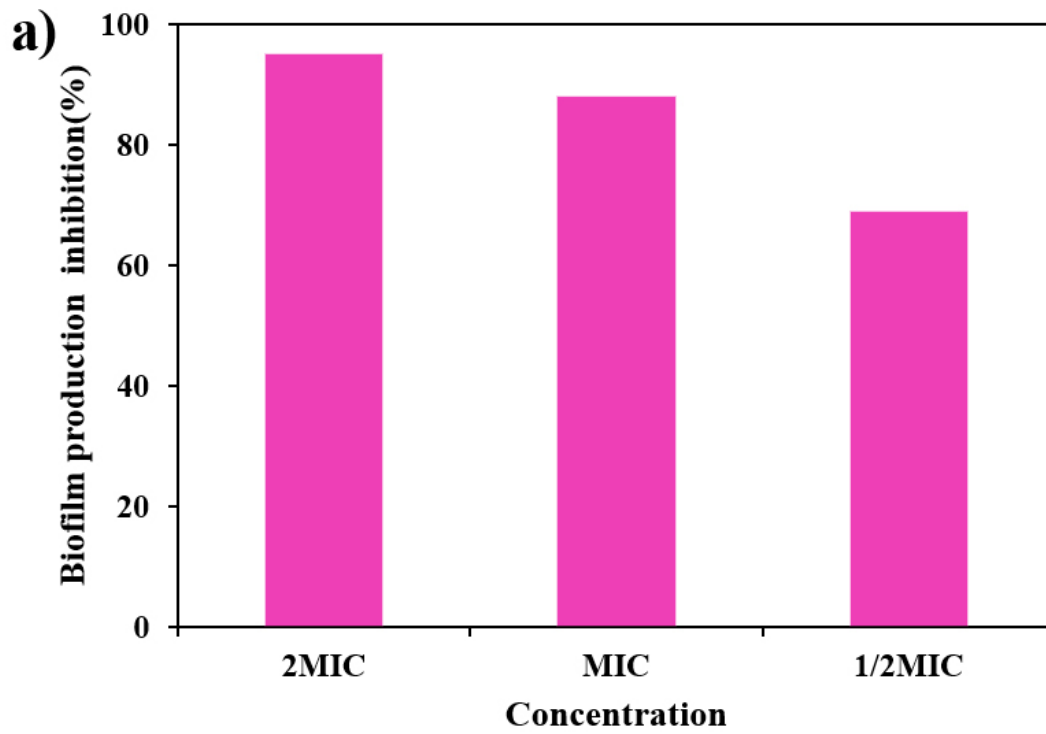


**Figure 7**

Effect of different concentrations of TI4HgI6 on biofilm formation by a) *Staphylococcus aureus* and b) *E. faecalis*. Assays were carried out in triplicate and the results were expressed as mean values  $\pm$  SD.

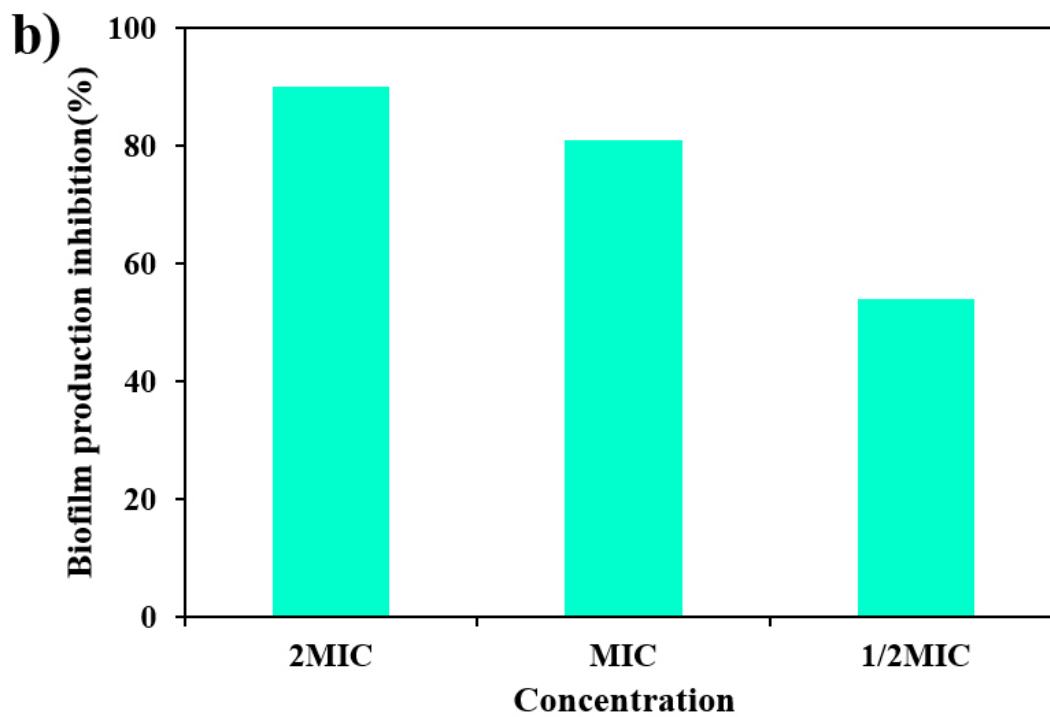
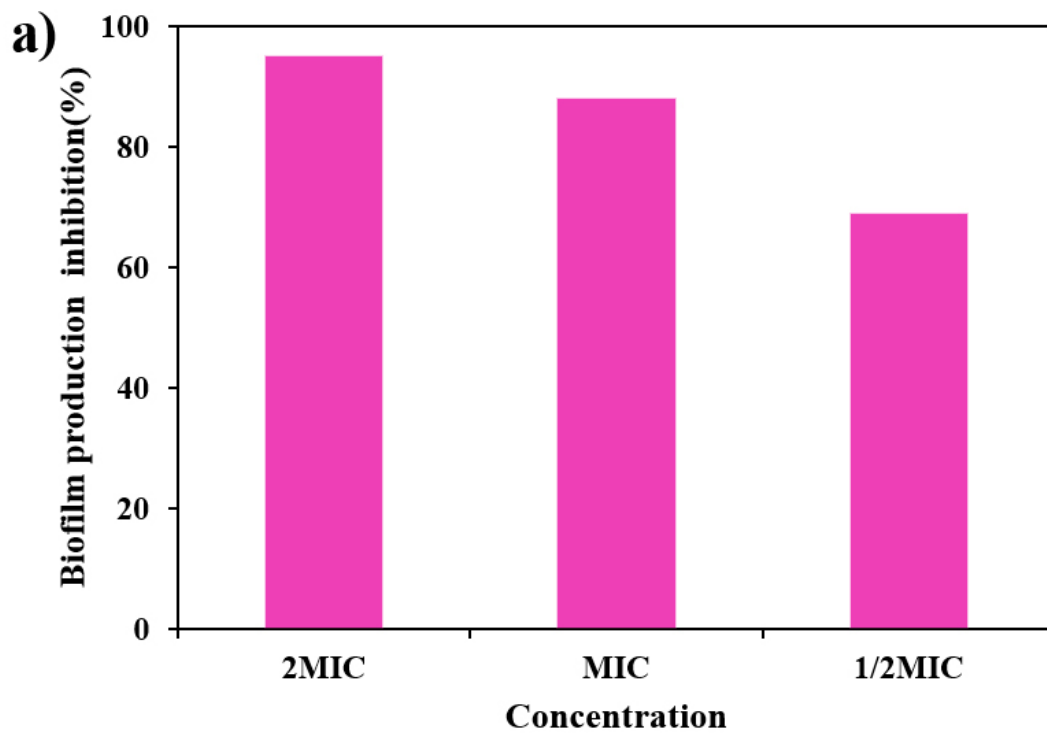


**Figure 7**

Effect of different concentrations of TI4Hgl6 on biofilm formation by a) *Staphylococcus aureus* and b) *E. faecalis*. Assays were carried out in triplicate and the results were expressed as mean values  $\pm$  SD.

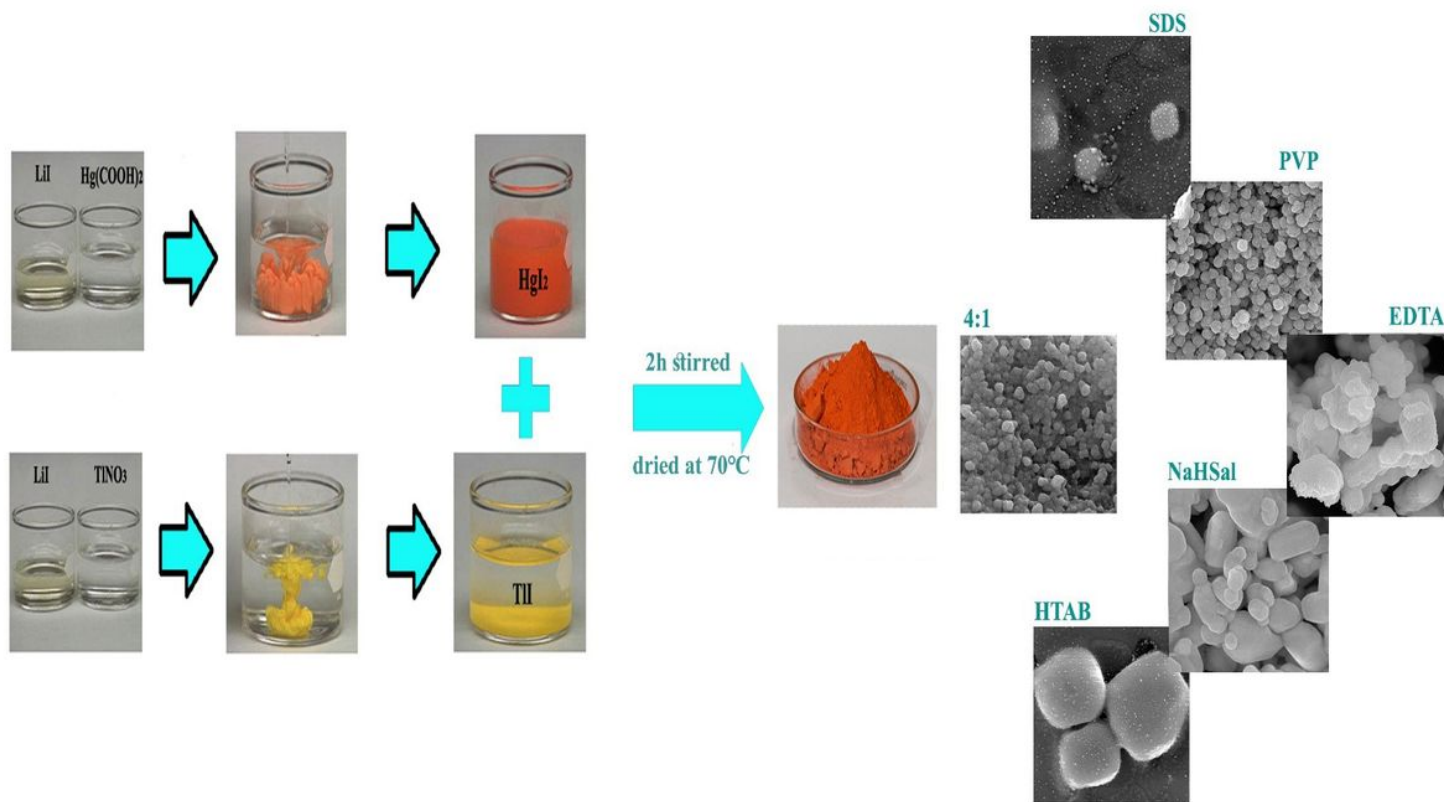


**Figure 8**

Schematic diagram of the fabrication of the nanostructures and the effect of capping agents on the particle size and morphology

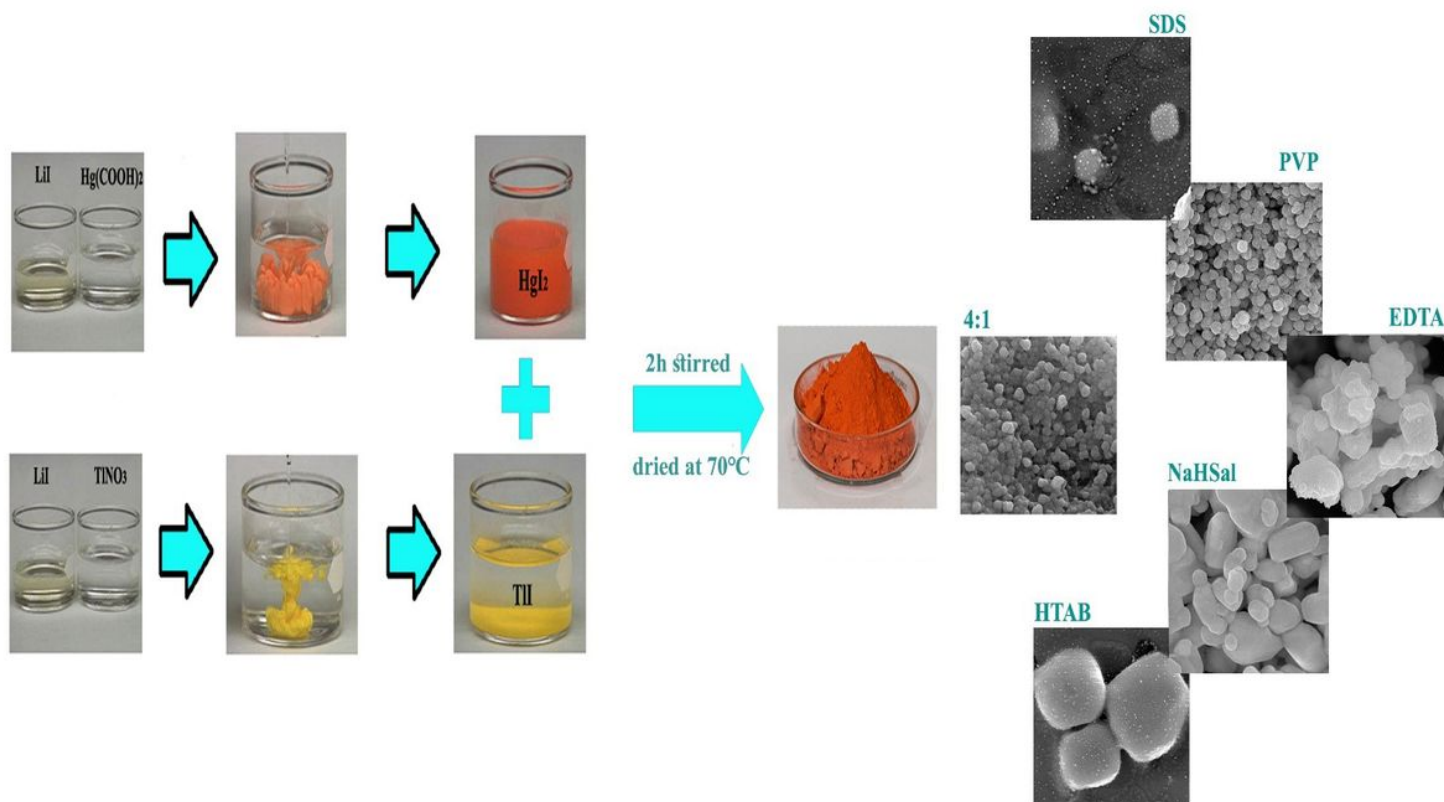


## Figure 8

Schematic diagram of the fabrication of the nanostructures and the effect of capping agents on the particle size and morphology